

Molecular docking and QSAR of aplyronine A and analogues: potent inhibitors of actin

Abrar Hussain · James L. Melville ·
Jonathan D. Hirst

Received: 4 August 2009 / Accepted: 22 October 2009 / Published online: 5 November 2009
© Springer Science+Business Media B.V. 2009

Abstract Actin-binding natural products have been identified as a potential basis for the design of cancer therapeutic agents. We report flexible docking and QSAR studies on aplyronine A analogues. Our findings show the macrolide ‘tail’ to be fundamental for the depolymerisation effect of actin-binding macrolides and that it is the tail which forms the initial interaction with the actin rather than the macrocycle, as previously believed. Docking energy scores for the compounds were highly correlated with actin depolymerisation activity. The 3D-QSAR models were predictive, with the best model giving a q^2 value of 0.85 and a r^2 of 0.94. Results from the docking simulations and the interpretation from QSAR “coeff*stdev” contour maps provide insight into the binding mechanism of each analogue and highlight key features that influence depolymerisation activity. The results herein may aid the design of a putative set of analogues that can help produce efficacious and tolerable anti-tumour agents. Finally, using the best QSAR model, we have also made genuine predictions for an independent set of recently reported aplyronine analogues.

Keywords Aplyronine A · Macrolides · F-actin depolymerisation · 3D-QSAR · AutoDock

Electronic supplementary material The online version of this article (doi:10.1007/s10822-009-9307-y) contains supplementary material, which is available to authorized users.

A. Hussain · J. D. Hirst (✉)
School of Chemistry, University of Nottingham, University Park,
Nottingham NG7 2RD, UK
e-mail: jonathan.hirst@nottingham.ac.uk

J. L. Melville
Cresset BioMolecular Discovery Ltd., BioPark Hertfordshire,
Welwyn Garden City, Hertfordshire AL7 3AX, UK

Introduction

Actin is a ubiquitous and highly conserved protein across many organisms [1]. In eukaryotic cells, it is distinctly abundant and one of the two main constituents of the cytoskeleton. Actin’s role as a cytoskeletal protein arises from its ability to assemble reversibly from its monomeric globular form (G-actin) into long polymers or filaments (F-actin) [2–5]. The dynamic nature of the actin cytoskeleton is critical for vital cellular functions, including determination of cell shape, cell motility, division and adhesion. These functions are monitored through the spatio-temporal regulation of actin filament dynamics by a plethora of endogenous actin-binding proteins (ABP) [6–8]. This strict and elaborate regulatory system governing actin filament dynamics can be vulnerable to mutations or changes in the expression levels of genes encoding an ABP [9]. Such events can result in critical fluctuations in the levels of F and G actin in the cytoskeleton. Given the functions fulfilled by actin, it plays a fundamental role in tumorigenic cells [10, 11]. For this reason, actin is a strategic target for anti-tumour therapy to correct or reverse the changes in the actin cytoskeleton [12, 13].

Further interest in actin has arisen through the discovery of several marine natural products (hereafter, simply referred to as macrolides) [10, 14], which exhibit ABP mimicking behaviour. This property, consequently, makes these molecules promising anti-cancer leads. Many of the macrolides have already demonstrated the ability to disrupt actin filament dynamics, which underlies their cytotoxicity against several strains of tumours [15–17].

The co-crystallised structures of several G-actin bound macrolides have been published [10]. However, out of at least six known macrolide binding sites on actin, a disproportionately large number of the compounds bind to the

barbed-end of actin, between subdomains 1 (SD1) and 3 (SD3) [10, 18]. This site is also known as the (+)-end, so called as the site at which polymerisation advances at a higher rate than the opposite end; the latter is known as the pointed or (–)-end. These compounds, which are members of the broad class of (+)-end binding macrolides, include aplyronines [19, 20], kabiramides [15, 17], reidispogiolides [21], ulapualides [22, 23] and several others [10]. Though the chemical structures of these compounds are highly variable, they do have two common characteristics: a macrocyclic ring and a long flexible side-chain, referred to as the “tail” [10, 14] (Fig. 1a). The tail binds between a narrow cleft separating SD1 and SD3, whilst the macrocycle positions itself on the so called hydrophobic patch, on the protein’s surface adjacent to the cleft (Fig. 1b).

Our focus is on the aplyronine family of compounds from the sea hare *Aplysia kurodai*. In 1993, the highly cytotoxic compounds: aplyronines A, B and C were isolated and their structures determined [24]. Of the three, aplyronine A exhibits the most potent anti-tumour and F-actin depolymerisation activity [20, 25]. Studies using fluorescence imaging techniques have shown aplyronine A, like other (+)-end targeting macrolides, inhibits actin polymerisation by sequestering G-actin with a 1:1 stoichiometry, whilst depolymerising F-actin by severing [26].

Past studies on the aplyronines have reported cytotoxicity against HeLa S₃ cells and the in vitro F-actin depolymerisation effect of 19 natural and synthetic aplyronine

Table 1 Cytotoxicity against HeLa S₃ cells and actin depolymerisation activity of the 19 aplyronine analogues as published in Kigoshi et al. [20]

Compound number	Cytotoxicity (pIC ₅₀)	Depolymerisation (pIC ₅₀)
Aplyronine A (1)	9.35	4.51
Aplyronine B (2)	8.54	4.48
Aplyronine C (3)	7.65	4.49
4	6.73	4.24
5	8.78	4.11
6	8.98	4.46
7	6.88	4.46
8	5.47	–
32	8.60	4.42
36	7.40	4.44
40	7.03	3.72
43	5.68	4.31
64	5.56	2.35
67	–	2.74
78	–	Inactive
85	7.26	4.15
89	–	2.12
102	–	3.48
111	–	3.34

N.B. Compound numbers used here and throughout this report correspond to those tested in Kigoshi et al. activity values have been converted to pIC₅₀ values of the molar concentrations

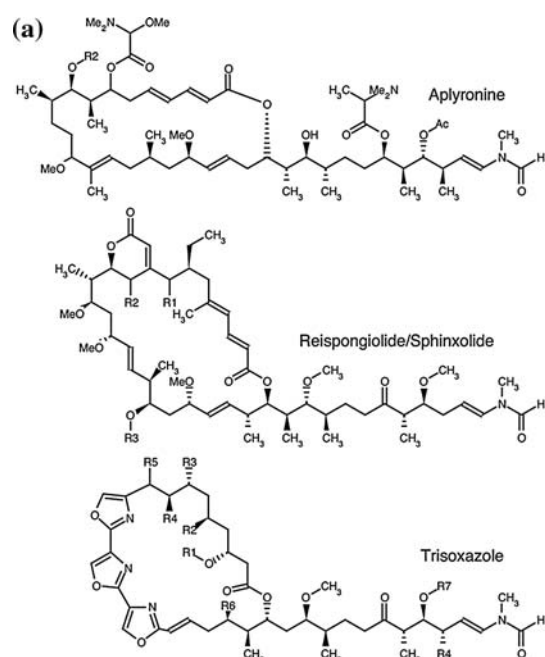
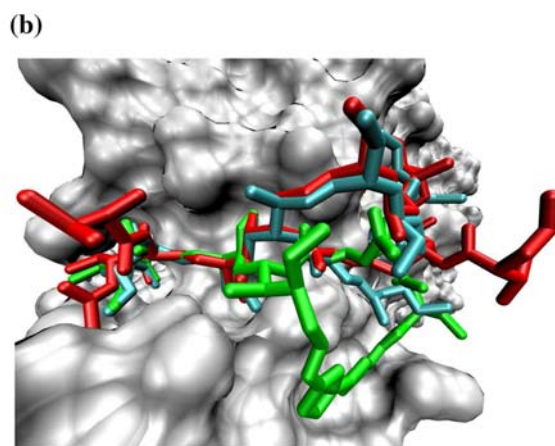


Fig. 1 (a) Molecular structure of 3 (+)-end binding macrolides. (b) Binding modes of aplyronine A (red sticks), kabiramide C (green sticks), and reidispogiolide A (cyan sticks) are shown superimposed



in their bound conformations on the (+)-end binding site of G-actin. Actin structure is shown as the grey surface representation model taken from the G-actin/aplyronine A complex (PDB code 1WUA)

analogues [20, 25] (Table 1). Subsequently, the authors commented on a number of structure-actin depolymerisation and structure-cytotoxicity relationships for selected analogues [19, 20]. However, those studies did not provide detail on the binding mechanism of each of the analogues to actin and its influence on cytotoxicity and F-actin depolymerisation. Herein, we investigate the binding modes of the 19 analogues, giving us a better understanding how binding may contribute to the bioactivity of each analogue. We also report on a 3D-QSAR study of these compounds using our implementation of the CoMSIA [27] approach to computing 3D descriptors. Our studies show a high degree of binding specificity in the tail over the macrocycle, challenging previous suggestions regarding the two-phase binding of the macrolides [15, 17]. These suggestions posit that the macrocycle of (+)-end macrolides initiate binding to a hydrophobic patch on the surface of actin, which is followed by the intercalation of the tail into a narrow cleft between SD1 and SD3, similar to the natural F-actin severing protein gelsolin [28, 29]. Our work also provides insight into the inhibitory mode of action of the aplyronines and may aid the design of new compounds against actin deregulation and cancer.

Materials and methods

Molecular modelling

Preparation of the target and ligands

We used a dataset of 19 compounds taken from Kigoshi et al. [20]. Although the dataset is rather small, these data are the most extensive, quantitative measurements on an actin-macrolide system to date. The limited number of compounds is mitigated by the availability of detailed structural data, which the computational analyses aim to augment. The structures of the compounds have been replicated, with corresponding compound numbers, in Table 2. A measure of the cytotoxicity for 14 compounds and actin depolymerisation activity for 17 compounds were taken from the Kigoshi et al. [20] at the given concentrations. These are given in Table 1 as pIC_{50} values of the molar concentrations. Each compound in the dataset was constructed using the molecular modelling package Spartan [30] and (locally) energy-minimized in vacuo, using the Merck molecular mechanics force field (MMFF) [31], to obtain reasonable geometries. The actin monomer used for the docking studies was taken from the co-crystallised structure of aplyronine A complexed with a G-actin monomer (PDB code 1WUA) [19]. Prior to initiating the docking simulations, all non-protein molecules were removed from the actin monomer. For any alternative atom locations only the first location ('A') was retained. All

non-polar hydrogen atoms were merged to the connecting heavy atom, leaving only heavy atoms and polar hydrogen atoms. Following this, AD4 atom types and Gasteiger-Marsili atomic charges [32] were assigned for the protein and each aplyronine analogue, using AutoDock Tools (ADT) [33].

Docking parameters

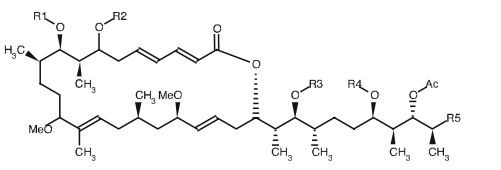
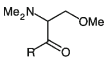
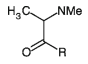
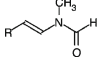
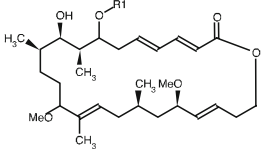
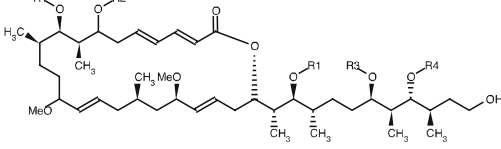
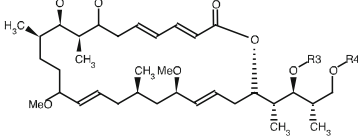
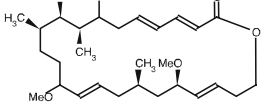
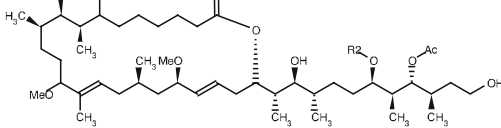
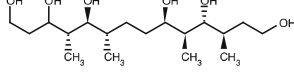
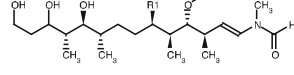
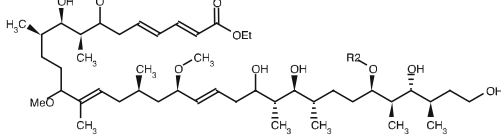
All docking simulations were carried out in AutoDock (v4) using the Lamarckian genetic algorithm [34, 35]. The target (actin monomer) for each docking was kept rigid, therefore assuming there is no induced conformational change upon ligand binding. This was a plausible assumption, given the C_α trace of actin monomers in several actin/macrolide complexes deviates only between 0.28 and 0.46 Å [36]. A similar observation was made by Hirata et al. [19]. In contrast to the protein, torsional flexibility was permitted for the ligands via the side-groups, whilst the macrocycle-tail backbone was kept rigid.

Atomic affinity and electrostatic potentials were computed for a grid box positioned around the approximate centre of the binding site, with dimensions $27.0 \times 27.0 \times 22.5$ Å. All other docking parameters remained as the AutoDock default settings, except the GA population size was increased to 300 and the number of energy evaluations per trial was set to 5×10^6 . The increase here was due to the large number of flexible torsions that are explored during simulation, which increase the search space for the more flexible compounds. Each flexible docking simulation was repeated for 100 trials per compound, yielding 100 docked conformations for each compound.

Evaluation of docking results

Results for each compound were classified by sorting all 100 docked conformations in increasing order of binding energy. Using the lowest energy conformation as a reference, poses with an RMSD within 2 Å of the reference pose were grouped into one cluster. The process was repeated for each remaining conformation, until all the 100 conformations belonged to a single cluster. A new reference conformation was defined every time a new cluster was created. Following this, the best-docked conformation is selected as the lowest energy pose in the most populated cluster, i.e., the cluster with the highest convergence out of the 100 trials. This differs from the practice of simply choosing the overall lowest energy pose. Thus, we avoid picking lower energy ranked poses belonging to sparsely populated clusters, which can be considered as 'chance-hits' given that the docking algorithm was unable to converge to similar poses in other independent trials.

Table 2 Molecular structures of aplyronine A and 18 natural and synthetic analogues

Structure	No.	Substituents				
		R1	R2	R3	R4	R5
	1	H		H		
	2	Me ₃ Ser	H	H	(Me ₂ Ala)	(MVF)
	3	H	H	H	Me ₂ Ala	MVF
	4	Ac	Me ₃ Ser	Ac	Me ₂ Ala	MVF
	5	H	Me ₃ Ser	H	Me ₂ Ala	MVF
	6	H	Me ₃ Ser	H	H	MVF
	7	H	H	H	H	MVF
	8	Me ₃ Ser	—	—	—	—
	32	H	Me ₃ Ser	Me ₂ Ala	Ac	—
	36	H	Me ₃ Ser	H	Ac	—
	40	H	Me ₃ Ser	H	H	—
	43	H	Me ₂ Gly	Me ₂ Gly	Ac	—
	64	Me ₂ Ser	Me ₃ Ser	Me ₂ Ala	Ac	—
	67	Me ₂ Ser	H	Me ₂ Ala	H	—
	78	Me ₃ Ser	—	—	—	—
	85	Me ₂ Ser	Me ₂ Ala	—	—	—
	89	—	—	—	—	—
	102	Me ₂ Ala	—	—	—	—
	111	Me ₂ Ser	Me ₂ Ala	—	—	—

Incorporation of binding site water molecules

To study the effect of water, each docking was repeated with the inclusion of explicit water molecules as part of the target protein. The scheme employed here was to incorporate only those water molecules which were conserved

and tightly bound to the actin monomer. This was reasonable, given that water molecules often occupy conserved sites in related proteins [37–40]. The enthalpy gain often outweighs the entropic penalty incurred by ordering of the water molecules. Therefore, conserved water molecules are not easily displaced upon ligand binding. For that

reason, conserved water molecules can potentially influence the binding mode of a ligand.

We searched for such conserved water molecules in the crystal structures of six other actin-macrolide complexes using the water molecules from the actin-aplyronine complex (**1**/G-actin) as a reference. The six complexes plus the **1**/G-actin complex were superimposed by RMSD minimization of the binding site C α trace. Any water molecules that were found at the same site as in the **1**/G-actin complex, in at least four of the other complexes, were judged as being conserved. All other water molecules were ignored, as were any conserved water molecules that were unable to form suitable hydrogen bonds to local protein residues. This left 11 water molecules as part of the docking target.

In order to carry out dockings to a target with explicit water molecules, the placement and orientation of the hydrogen atoms is important. Hydrogen atoms were added to the oxygen atoms of the 11 water molecules. These were manually optimised, to form hydrogen bonds with the protein. This was followed by several rounds of energy minimization, in the presence of the protein, using the Szybki molecular optimisation tool [41], to ensure all the water molecules made optimum hydrogen bonds with the protein. The locations of the water molecules in the binding site are shown in Fig. 2.

Structure-activity analysis

The premise of a QSPR/QSAR is that specific properties of a molecule, which are known to influence a molecule's activity, are determined by its structure. Those properties can be represented by measurable parameters, such as log*P* for lipophilicity, to establish a relationship in the form of an equation between the structure and activity of the

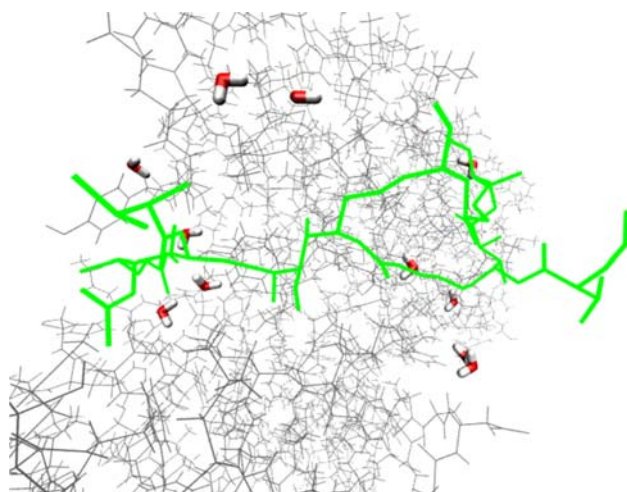


Fig. 2 Position of conserved water molecules (red and white sticks) on the surface of the (+)-end binding site of actin (grey). The bound conformation of **1** is shown as a reference

molecule. These models can be used to predict the activity of novel structures in the series and perhaps contribute to a decision as to which set of molecules to synthesise. For our work we carried out a traditional field-based 3D QSAR approach derived from the popular CoMSIA [27] technique. The study was carried out on a dataset of 17 (of the 19) aplyronines for which depolymerisation measurements were available, see Table 1.

3D QSAR methodology and interpretation

All 3D-QSAR analyses were performed with an in-house version of CoMSIA descriptors. Four property types were evaluated: electrostatics, steric effect, lipophilicity, and solubility. The electrostatic properties were represented by Gasteiger partial charges [32], the steric effects by molar refractivity [42], lipophilicity by log*P* [42], and solubility by log*S* [43]. Prior to generating the descriptors, atomic property values were assigned to each atom in the dataset. A crucial first step in 3D-QSAR is to determine the active conformations of each molecule in the set and apply a suitable alignment criterion in order to quantify the changes at analogous positions across members of the set. Focussing only on the depolymerisation set, we used the best-docked conformations taken from the docking simulations carried out on each compound (in presence of water). In the absence of an experimental structure for the analogues (except **1**), the best-docked conformation of each analogue was considered to be the closest to the true active conformation and therefore used. Each compound was then aligned, using the Tcl interface in VMD [44], by least-squares fit of the rigid macrocycle and tail C-backbones (Fig. 3).

Descriptors were calculated on a regular lattice, with a grid resolution of 1.0 Å. The lattice dimensions were set to enclose all the aligned compounds with a margin of 4.0 Å in each dimension, to give a grid of 18,711 points. Each field value was allocated using a distance-dependent Gaussian-type function:

$$G_{pj}(c) = \sum_{i=1}^n P_i e^{-\alpha r_{ij}^2} \quad (1)$$

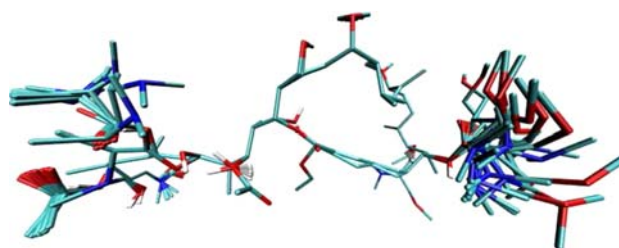


Fig. 3 Structural alignment of 17 aplyronine analogues in the depolymerisation set according to a least-squares fit of the backbone carbon atoms

Table 3 Results of docking simulations using flexible ligands

	No.	Torsions	No. of clusters ^a	RMSD ^b (Å)	Members in cluster	Rank of cluster	E_{docked}^c (kcal/mol)
	1	18	16	1.14	76	1	−13.9
	2	18	24	2.09	18	2	−10.0
	3	13	2	1.08	99	1	−13.8
	4	20	27	1.39	26	1	−11.5
	5	18	16	1.20	80	1	−13.1
	6	15	1	1.10	100	1	−13.5
	7	10	1	0.94	100	1	−13.2
	8	9	34	8.83	12	1	−8.0
	32	18	14	1.34	76	1	−13.0
	36	15	2	1.11	99	1	−12.7
	40	14	1	1.14	100	1	−11.7
	43	16	7	1.14	93	1	−13.2
	64	12	12	1.23	57	1	−8.3
	67	14	33	1.70	40	1	−9.2
	78	9	29	8.77	20	2	−7.8
	85	18	15	1.31	73	1	−13.2
	89	7	21	4.73	41	2	−7.9
	102	11	33	1.28	17	1	−9.6
	111	17	19	1.36	41	1	−9.8

The last four columns are specific for the lowest energy conformation in the most populated cluster (i.e. best conformation)

^a Indicative of the total number of binding modes produced

^b RMSD of best docked conformation with respect to the reference conformation

^c AutoDock binding energy of best docked conformation, with entropy term ignored

where G_{pj} is the field value of property p at grid point j for compound c ; i is the atom index; P_i is the atomic property of atom i ; α is the attenuation factor which is set at 0.3; r_{ij} is the distance between atom i and grid point j .

Following descriptor calculations, partial-least-squares regression (PLS) was used to construct the QSAR models. The final model was selected and validated using leave-one-out (LOO) cross-validation (CV) at the first minimum in the standard error of cross-validation (S_{PRESS}). To visualise the SARs encoded in the derived 3D-QSAR model, contour maps were generated by interpolating the product of the PLS coefficient and the standard deviation of the 3D field descriptor, to produce “stdev*coeff” fields. These fields best explain the relationship between variations in the spatial property of a molecule and changes in the activity. Since we were interested only in descriptors with the most significant influence on the activity of a compound, an equivalent percentage enclosing the lowest and highest field values was extracted from the fields. These extreme field values are indicative of the sign and magnitude of the corresponding QSAR term. When these values are plotted in space, they accordingly represent the spatial regions where appropriate substituent groups on a molecule will enhance the activity and regions where less favourable substituents are detrimental to the activity of a molecule. All four field maps were generated for the top and lower 20% contribution levels. The maps were viewed as isocontours using VMD [44]. All images throughout this

paper were produced using VMD and POV-Ray (<http://www.povray.org/>).

Results and discussion

Docking analysis

The experimental structure of aplyronine A (**1**) was used as a control to establish the optimum set of AutoDock docking parameters for the simulations, by re-docking the compound to the actin monomer, without torsional flexibility. The control docking using the optimum parameters produced a conformation with an RMSD of 0.73 Å from the crystal structure. Flexible docking simulations were performed on each compound, giving torsional freedom to all functional groups branching off the macrocycle/tail C-backbone. This produced up to 20 flexible torsions for the more flexible compounds and as few as seven for the smaller analogues (Table 3). The resulting conformers of each compound were clustered according to the homogeneity in the final binding modes and the binding energy scores. For each compound the lowest energy conformation from the most populated cluster was considered to be the most likely actin-bound conformation and on that basis predicted as the active conformation. Each cluster is representative of a different binding mode.

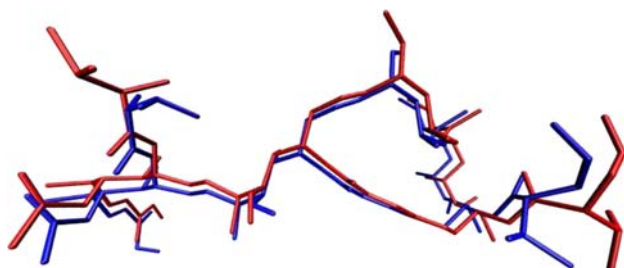


Fig. 4 Comparison of best docked conformation of aplyronine A (*blue*) to G-actin and the experimental bound conformation (*red*). The RMSD is 1.14 Å

The best docked conformation of **1** agreed with the crystal structure to an RMSD of 1.14 Å (see Fig. 4; Table 3). For all but three compounds, the best docked conformation was taken from the first cluster. Although several alternative binding modes were produced for many compounds, the most populated cluster was often much larger than any other cluster. The cluster cut-off was 2.0 Å. Compounds **6**, **7**, and **40** all converged to just a single cluster from 100 docking trials. Somewhat surprisingly, this was not the case for compound **1**. The high convergence for compounds **6**, **7** and **40** was possibly due to the absence of the di-methyl alanine (Me₂Ala) moiety on the tail (see Table 2), which perhaps allows the tail to intercalate more easily into the SD1/SD3 cleft.

We compared the best-docked conformations of each ligand to the spatial coordinates of the pre-docked ligands. These pre-docked structures were placed in the same frame of reference as that of the co-crystallised structure of **1**. From this we learned that analogues with both a macrocycle and a tail docked well within 2.0 Å of their reference conformations, with the exception of **2**, which docked with an RMSD of 2.09 Å from its reference (Table 3). 2.0 Å is often considered as a good “hit” when comparing conformations [45]. This high number of macrocycle/tail analogues taking up binding modes similar to aplyronine A

was no surprise given the diverse structures of the macrolides that are accommodated by the binding site [10, 14] (Fig. 1).

Interestingly, the best-docked conformations of the macrocycle analogues (**8** and **78**) were distinctly different from their reference structures. In fact, both docked at the entrance of the vacant hydrophobic cleft with respective RMSDs of 8.83 and 8.79 Å from their reference positions, on the hydrophobic patch (Fig. 5). Compared to the best docked conformation, the closest docked conformation (RMSD 1.40 Å) for compound **8** to its reference had a 2.0 kcal/mol higher docking energy score, in cluster 17; the closest for **78** (RMSD 1.72 Å) was 1.8 kcal/mol higher energy, in cluster 18.

In contrast, the best conformations of both tail-only analogues (**89** and **102**) were able to dock at the hydrophobic cleft, independent from the macrolide ring. This is particularly revealing given the best conformation for the macrocycle analogues failed to bind to the patch. This observation prompts us to question the sequence in which the two-phase binding mechanisms of these macrolides occurs. Previous spectroscopic studies on the trisoxazoles showed the macrolides to bind to actin via a two step-reaction, where the tail and macrocycle bind independently [15, 17]. The authors conjectured the macrocycle binding corresponded to the first phase and the tail to the second phase. However, our observations indicate that there is little binding specificity in the macrocycle for the hydrophobic patch and much of the specificity lies in the tail. Therefore, it is unlikely that the macrocycle can independently bind to actin ahead of the tail. Moreover, it is possible that the macrocycle merely anchors itself on the patch to stabilise the actin-macrolide interface after the tail is securely bound in the cleft.

Both compounds **89** and **102** were simulated in larger grids compared to the other analogues to explore their propensity to bind deeper into the SD1/SD3 cleft. **102** failed to

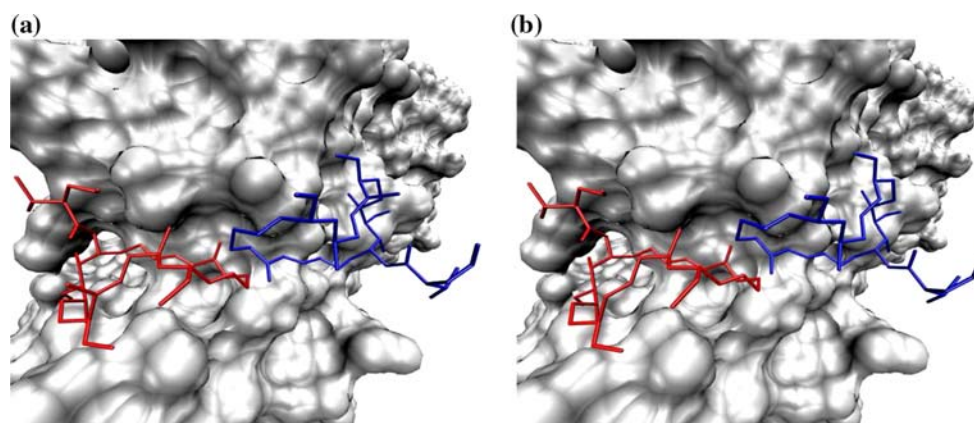
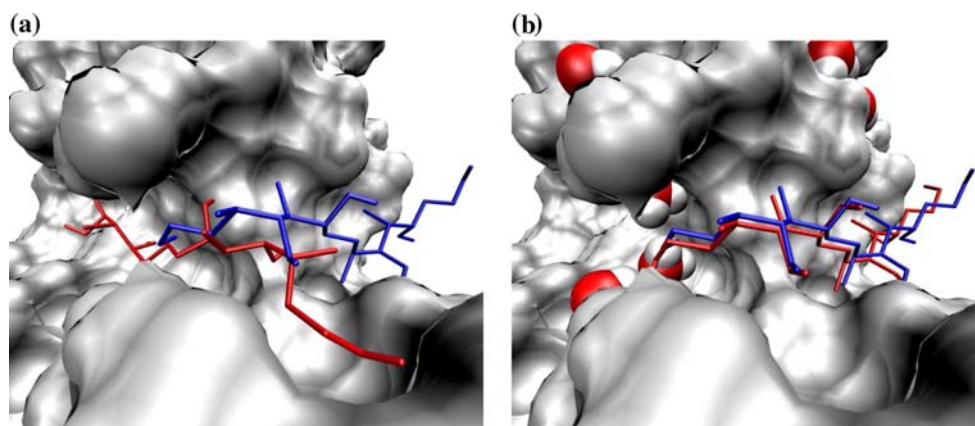


Fig. 5 Overlay of the best docked conformation (*red*) of compounds (a) **8** and (b) **78** superimposed in the (+)-end binding site. Reference poses are shown in *blue*

Fig. 6 Overlay of the best docked conformation of compound **89** (red) superimposed in the SD1/SD3 cleft (a) in a water-free receptor and (b) in presence of water molecules, shown as vdW spheres. Reference conformations are shown in blue. The hydrophobic path is around the right-hand side of the cleft



intercalate further along the cleft, due to the large Me₂Ala moiety blocking further intercalation via the entrance to the cleft. On the other hand, the relatively simple structure of the hexaol analogue (**89**) did bind deeper (Fig. 6a), with a 0.7 kcal/mol lower binding energy than the docked conformation closest to the reference structure.

Incorporation of explicit water molecules

We also investigated simulating the ligands in a binding site in presence of explicit water molecules. All dockings in the presence of water were carried out using the same parameters used for the water-free receptor. A total of 11 water molecules were included, bound to the receptor as shown in Fig. 2. Overall, there was little change in the binding modes of the best docked conformation of each ligand compared to the results from the water-free simulations (see Δ RMSD in Table 4). There were three exceptions to this. The first was compound **2**, which docked 0.25 Å closer to its reference structure. This difference was primarily due to a translational shift in the compound, to allow the *N*-methyl-*N*-vinylformamide (MVF) moiety at the tail terminus to hydrogen bond to two water molecules in the SD1/SD3 cleft (Fig. 7a, b). As a result of acquiring the enthalpically favourable hydrogen bonds, the binding energy also decreased. The second difference was in the binding mode of **4**, which, compared to the docked conformation in absence of water, also docked 0.25 Å further from its reference, as shown in Fig. 7c. As in the case of **2**, this 0.25 Å deviation was also a result of the formation of the same water-mediated interactions (Fig. 7d). Lastly, **89** had moved out of its buried position deep in the cleft, as seen in Fig. 6a, and docked at 1.02 Å from its reference structure (Fig. 6b), i.e., close to the site of the macrolide tail of **1**. The difference in the position, which also resulted in a higher docking energy score, occurred due to a small group of three conserved water molecules hydrogen bonded to the backbone amides of Val134, Ile136 and Ala170 in the SD1/SD3 cleft. These

water molecules act as a barrier preventing ligands penetrating further down the cleft, as shown in Fig. 6b.

Although there was little difference between the docking in the water and water-free scenarios, there were some differences in the docking energy scores (see ΔE_{docked} in Table 4). This was particularly noticeable for compounds possessing a terminal MVF moiety (Table 2), which docked with a lower energy than in a water-free receptor. As mentioned above for compound **2**, the decrease in binding energy here was also caused by the enthalpy gain through two water-mediated interactions (HOH9 and HOH15) bridging Ile136 and Ala170 and the MVF moieties. Excluding **4**, the average decrease in E_{docked} for compounds with an MVF moiety was -0.6 kcal/mol (see ΔE_{docked} in Table 4). For compound **4**, which also has a MVF moiety, the decrease is not apparent, since the shift in the docking position that was required to make the water-mediated interactions neutralised this energy gain at another region of the protein-ligand interface. In contrast to compounds with an MVF moiety, there was a small increase in E_{docked} for some of the remaining compounds with an intact tail (**5**, **32**, **36**, **40**, **43**, **85** and **102**). This difference in the energy was again attributed to the same water molecules, but on this occasion resulted in an increase, due to the repulsion between the partial positive charges on the hydrogen atoms of the water molecules and the hydroxyl at the tail terminus (in place of the MVF moiety).

Correlation between activity and docking energy

The binding energies of the best docked conformations correlated with actin depolymerisation activity, with an r^2 coefficient of 0.76 ($n = 17$). However, only limited correlation was seen between the binding energy and cytotoxicity, r^2 of 0.33 ($n = 14$). The correlations increased following docking simulations with the conserved water molecules, giving r^2 values of 0.80 and 0.40, respectively. This difference in the values between these two sets could be due to other factors affecting the cytotoxicity of the

Table 4 Results of docking simulations using flexible ligands in presence of explicit water molecules

No.	No. of clusters	RMSD ^a (Å)	Members in cluster	Rank of cluster	E_{docked} ^b (kcal/mol)	ΔRMSD ^c (Å)	ΔE_{docked} ^d (kcal/mol)
1	12	1.21	79	1	−14.6	0.07	−0.7
2	23	1.84	22	2	−10.6	−0.25	−0.6
3	2	1.09	97	1	−14.4	0.01	−0.5
4	33	1.65	20	1	−11.5	0.25	0.0
5	15	1.29	79	1	−13.1	0.09	0.0
6	1	1.08	100	1	−14.1	−0.02	−0.6
7	1	0.86	100	1	−13.9	−0.08	−0.7
8	26	8.79	13	1	−7.7	−0.05	0.3
32	15	1.29	77	1	−13.0	−0.05	0.0
36	1	1.09	100	1	−12.5	−0.02	0.2
40	1	1.14	100	1	−11.6	−0.01	0.2
43	8	1.22	90	1	−13.1	0.08	0.1
64	14	1.33	56	1	−8.5	0.10	−0.1
67	16	1.51	34	1	−9.1	−0.19	0.1
78	22	8.82	21	2	−7.8	0.06	−0.0
85	11	1.28	82	1	−13.1	−0.02	0.2
89	27	1.02	37	3	−7.2	−3.71	0.7
102	34	1.15	14	1	−10.1	−0.13	−0.6
111	17	1.50	37	1	−9.5	0.14	0.3

Columns 3–6 are specific for the lowest energy conformation in the most populated cluster (i.e., best conformation). The last two columns are the differences between the results in presence and in absence of water molecules (Δ = with water – without water)

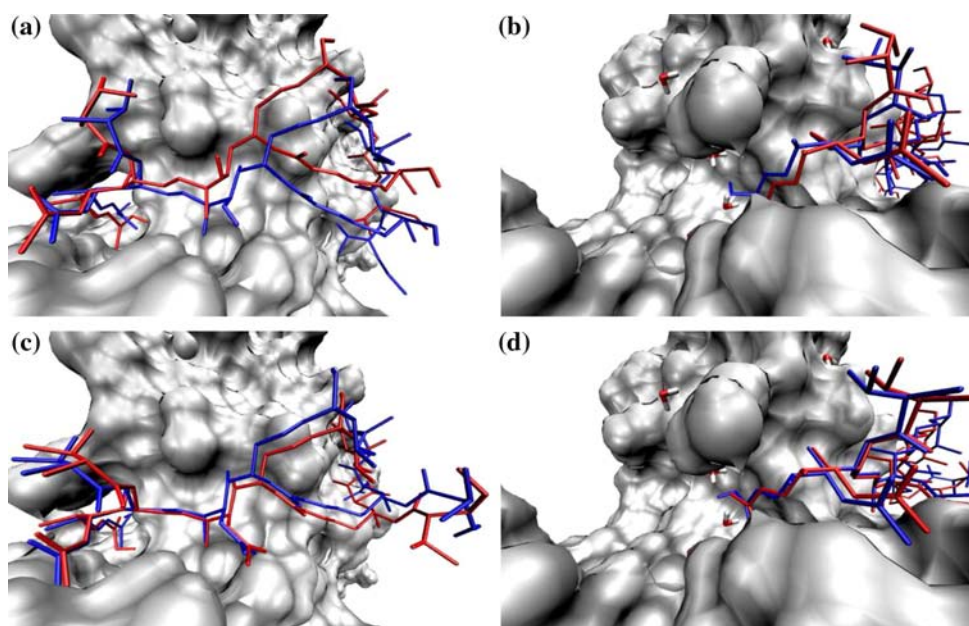
^a RMSD of best docked conformation with respect to the reference conformation

^b AutoDock binding energy of best docked conformation, with the entropy term ignored

^c RMSD difference between best docked conformation in presence and in absence of water molecules

^d Energy difference between best docked conformation in presence and in absence of water molecules

Fig. 7 Overlay of the best docked conformations of (a) **2** and (c) **4** docked in presence (blue) and in absence of water (red). (b) and (d) show an overlay of **2** and **4**, respectively, in the SD1/SD3 cleft with water molecules shown



compounds. As seen from the original activity data (Table 1), the cytotoxic potency of the compounds is much greater than the depolymerisation activity, even

though the depolymerisation of F-actin is believed to be the basis for the cytotoxicity [16, 46]. With respect to the cytotoxicity measurements, the inconsistency between

the two measures may suggest that other factors, such as the membrane transfer or metabolism of the compounds may contribute towards the cytotoxic response. There may also be a disparity in the mode of action of the compounds within the cell where the compounds perhaps exert their cytotoxic response by involving additional proteins and/or signalling pathways.

Analysis of structure-activity relationships

Evaluation of 3D QSAR models

Given the higher correlation between depolymerisation activity and docking energy and an uncertainty over the exact mechanism by which the compounds exert their cytotoxic response, we only generated models for the depolymerisation data. Models were generated to consider all four property types individually and for all possible combinations to yield a total of 15 models. Statistics for all models are provided as Supplementary material; they are shown in Table 5 for the top five models. These models were selected according to predictive ability (q^2) for models using less than five components. All five gave comparable q^2 values, differing by less than 0.05. Since r^2 generally increases with the number of components [47], the best model was selected by scaling the r^2 values by the number of components used to construct the model. This revealed the combined model of all four properties as the best model, with a q^2 value of 0.85 at the second component. Since the combined property model was considered as the best and also provides more insight into the spatial features, of each property, that are important for activity, we focus on this model hereafter.

In absence of an external set of compounds to test our model on we carried out a y-randomisation analysis to validate the model further. For this, we built 300 independent models using the original descriptor pool and

randomly shuffled activity values. This established technique evaluates the risk of chance correlations in the original model [48]. To verify the robustness of the original model, the models built using permuted activities should have lower q^2 and r^2 statistics than the original [49]. The average q^2 and r^2 values over the 300 models were 0.04 and 0.08, respectively. Out of the 300 permuted activity models only 43 models gave q^2 values greater than zero. Figure 8 shows the relationship between the r^2 and q^2 for the randomised activity models that had non-zero q^2 values. Only four of these models had q^2 greater than 0.5, the highest of which was 0.64. Thus, we can be confident our real model is predictive.

Evaluation of 3D QSAR contour maps

To identify the features responsible for changes in depolymerisation activity, field contributions to the QSAR equation were visualised for each property. Starting with the electrostatic properties, Fig. 9a shows the contour map with compound **1** superimposed to aid visualisation. Red isopleths enclose regions where an electropositive substituent should enhance F-actin depolymerisation, which coincide with the slightly electropositive methyl of the esterified acetyl group (left of Fig. 9a). The blue isopleths represent regions where electronegative groups are required to increase activity, as seen by the blue contour near the carbonyl oxygen of the Me₃Ser group. In comparison to a less active analogue, like compound **64**, the reduced level of activity coincides with the presence of the α and β carbon atoms of Me₃Ser (where an electronegative substituent is expected) and the absence of an electropositive substituent at the red contour (Fig. 9b).

The contour map for the steric properties depicts green isopleths, representing regions where steric bulk confers increased levels of activity and yellow isopleths, enclosing areas where increased bulk is detrimental to the activity of

Table 5 Statistical data for 3D-QSAR analyses of depolymerisation

	Electrostatic + steric + lipophilicity + solubility	Electrostatic + steric + solubility	Electrostatic + solubility	Steric + solubility	Solubility
q^2 ^a	0.85	0.87	0.86	0.90	0.88
S_{PRESS}	0.35	0.34	0.35	0.31	0.34
ONC ^b	2	3	3	4	4
r^2 ^c	0.94	0.98	0.98	0.98	0.98
SEE ^d	0.19	0.10	0.10	0.10	0.10

^a Leave-one-out cross validated correlation coefficient

^b Optimum number of components

^c Non-cross validated correlation coefficient

^d Standard error of the model residuals

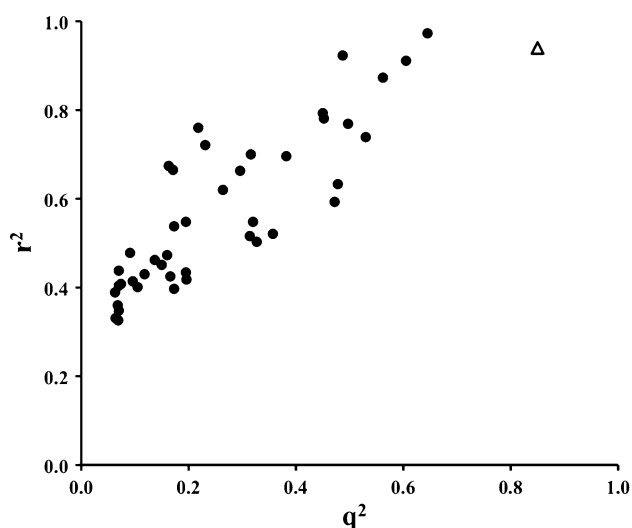


Fig. 8 r^2 against q^2 for the 43 y-randomisation models with q^2 values greater than zero (black dots). The triangle represents the real model

a compound (Fig. 10). In contrast to the electrostatic map, the steric fields provide a more detailed insight into the property. By superimposing compound **1** onto the map, we can see a long green isopleth stretching along the bulk of the tail, from C30 to the MVF terminus. In addition, there are two further bulk favouring isopleths: at the methyl group of the acetyl substituent and at the location of the Me₂Ala group. By viewing these fields in the binding site, we can see that agreement with these isopleths provides key interactions between the ligand and protein interface. Figure 10c shows the elongated green isopleth, which encloses the tail of compound **1**, comfortably fits in the SD1/SD3 cleft, lined by three tyrosine residues: Tyr133, Tyr143 and Tyr169 (coloured green) and Met355 (bottom left, coloured yellow). The smaller green isopleth, which encloses the acetyl carbon, fits in a hydrophobic pocket created by Leu346, Leu349 and Phe352 (leucines are coloured a light-pink shade towards the bottom middle).

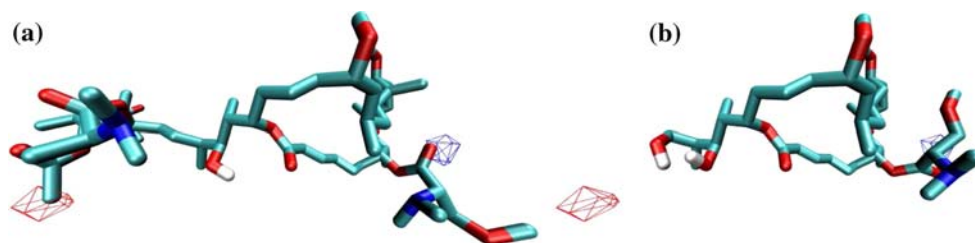
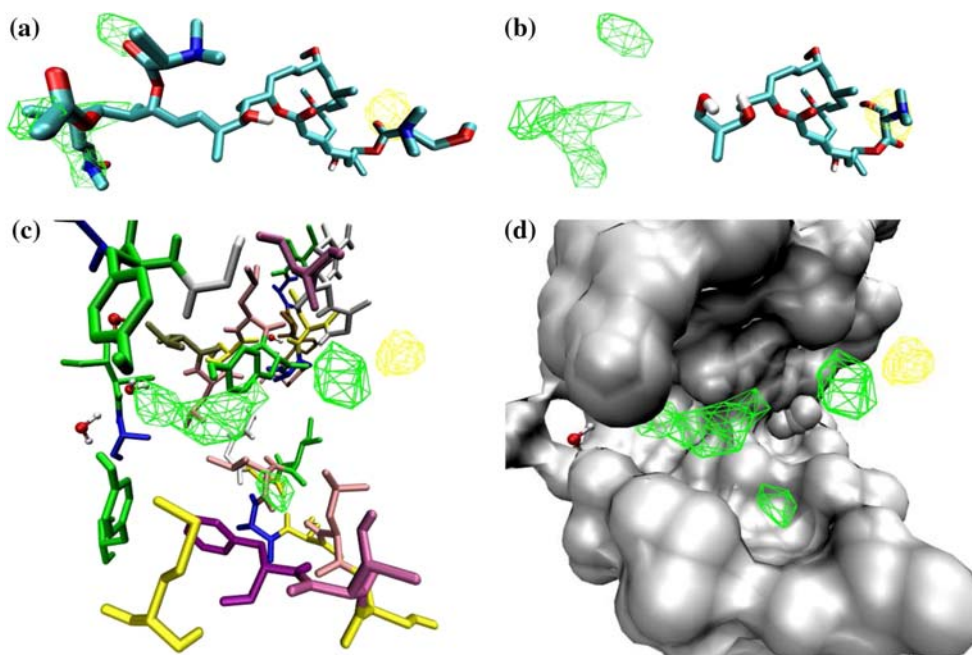


Fig. 9 3D-QSAR (stdev*coeff) contour map for the electrostatic properties. The red isopleths enclose regions where electropositive substituents enhance the depolymerisation activity, and blue isopleths

enclose regions where electronegative groups increase activity. To aid interpretation, superimposed on the fields is (a) the most active compound, **1** and (b) compound **64**

Fig. 10 3D-QSAR contour map for the steric properties. The green isopleths enclose regions where steric bulk is needed for increased activity, and yellow isopleths enclose regions where less bulk is required for increased activity. Superimposed on the map are compounds (a) **1** and (b) **64**. (c) and (d) show an overlay of fields in the binding site in a stick representation, coloured by residue name, and a surface representation, respectively



Furthermore, according to the docking data for compound **1** the binding of this methyl group contributes -0.5 kcal/mol to the docking energy score, which is the fourth largest enthalpic contribution out of the 76 heavy atoms. The significance of the location of the two aforementioned contours is emphasised in Fig. 10d. The yellow isopleth, which lies in a solvent-exposed region (Fig. 10d), encompasses the carbonyl group of the Me₃Ser group and excludes the bulk of this substituent. In contrast to compound **1**, the bulky Me₃Ser of analogue **64** enclosed by the solvent-exposed yellow contour and the absence of bulk in any of the green contours (Fig. 10b) are both partly attributed to the reduction in activity, with respect to other properties.

The contour map for the solubility properties displays orange isopleths to represent regions where substituents that increase solubility enhance the activity and green isopleths as regions where solubility enhancing substituents decrease activity. Again, by superimposing compound **1** we can see a large orange contour mostly occupied by the hydrophilic carbonyl oxygen of the Me₃Ser group and a solubility reducing ester bond of O-acetyl enclosed by a green isopleth, which both correlate with an increased

activity (Fig. 11a). Comparing this to compound **40**, which also has an intact macrocycle-tail backbone but is over 50% less active than **1**, we find a highly soluble hydroxyl group encapsulated by the green contour to result in a decrease in activity (Fig. 11b).

Finally, the contour map for the lipophilicity properties is depicted using black and grey isopleths, which enclose lipophilic and hydrophilic substituents, respectively, for increased activity. For the lipophilic contours we see a black isopleth encompassing the methyl of the acetyl group of compound **1** (Fig. 12a), which coincides with the small hydrophobic pocket on the protein surface that was seen using the steric map (see Figs. 10c, 12c). The grey contours, which enclose several hydrophilic groups also correlate with the increased activity of **1**. From left to right, on Fig. 12a there is a small grey isopleth at the MVF moiety, which is positioned between three polar tyrosine residues Tyr133, Tyr143 and Tyr169 and three water molecules in the binding site (Fig. 12c). This moiety contributes -2.3 kcal/mol to the enthalpic term of the docking energy score of compound **1** given in Table 4. Two larger grey isopleths encapsulate the two esterified amino acid moieties (Fig. 12a), which are coincidentally directed towards the

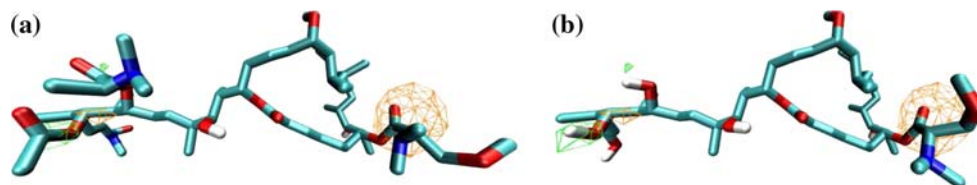
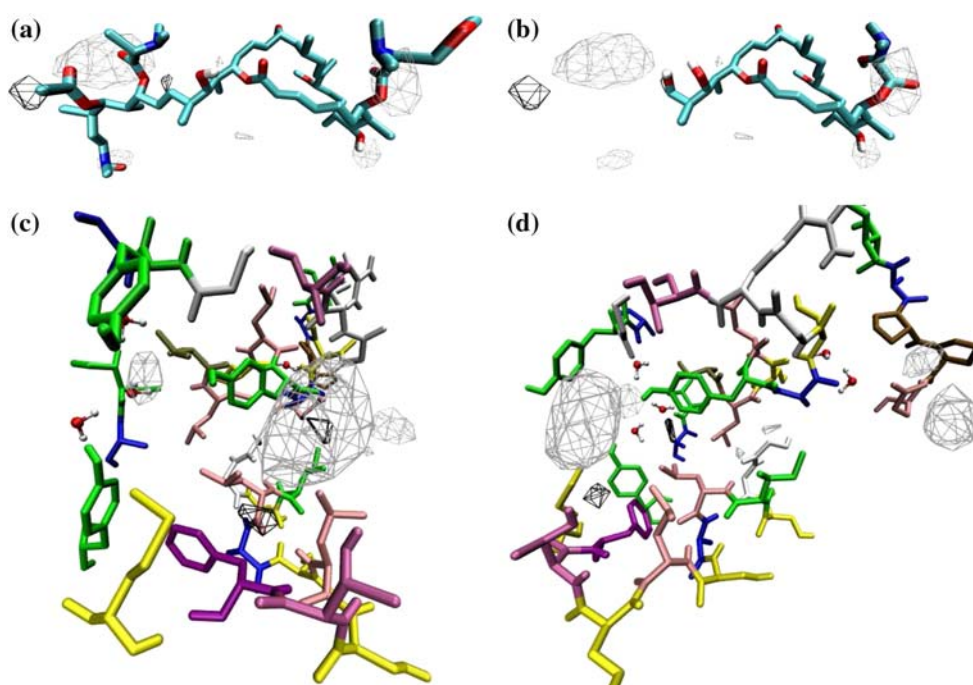


Fig. 11 3D-QSAR contour map for the solubility properties. The orange isopleths enclose regions where solubility enhancing substituents increase activity, and green isopleths enclose regions where

solubility decreasing substituents increase activity. Superimposed on the map is (a) compound **1** and (b) **40**

Fig. 12 3D-QSAR contour map for the lipophilicity properties. The black isopleths enclose regions where lipophilic substituents increase activity, and grey isopleths enclose regions where hydrophilic substituents increase activity. Superimposed on the map is (a) compound **1** and (b) **64**. (c) and (d) show an overlay of the fields in the binding site shown as sticks from a viewpoint at the SD1/SD3 cleft and the hydrophobic patch, respectively



solvent exposed region (Fig. 12c, d). The hydrophilic contour around the Me₃Ser moiety is also in accordance with the solubility enhancing contour on the solubility map. Another smaller hydrophilic contour encloses the hydroxyl group at C9 of **1** (second from right on Fig. 12a). This group forms a hydrogen bond with the polar Glu334 residue of actin (middle-right on Fig. 12d, coloured pink), which contributes -0.9 kcal/mol to the docking energy score. Viewing the map with respect to compound **64** shows an absence of substituents at three activity enhancing isopleths satisfied by compound **1** and the presence of a hydroxyl group at a small black isopleth where a lipophilic group is favoured. This all contributes to the decreased activity of **64**.

Predictivity of the 3D QSAR model

The predictive ability of the best model was checked using an external set of ten compounds (Table 6), nine of which only came to our attention after the completion of the initial QSAR study. This set consisted of five compounds (**A–E**) taken from Yamada et al. [50], four compounds (**F–I**) taken from Kitamura et al. [51] and the macrocycle analogue (compound **8**) that was excluded from the training set. As with the training set, each compound was first docked to actin to get an actin-bound conformation for each compound. Following the alignment of the bound conformations, descriptors were calculated on the 1.0 Å lattice used for the training set. Using the best QSAR model, values for depolymerisation activity were predicted as given in Table 7.

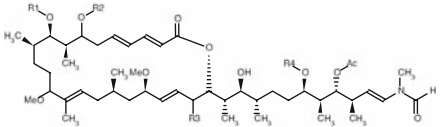
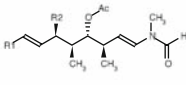
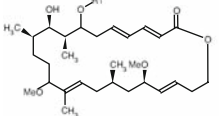
It is not possible for us to validate the predicted values, since, at the time of writing, there are no experimental values reported using the same assay conditions as used for the training set. However, the predictions seem reasonable, based on our findings herein. As expected, compounds

Table 7 Predicted depolymerisation activity for external set of molecules

Compound	Depolymerisation (pIC ₅₀)
A	4.48
B	4.53
C	4.43
D	4.32
E	4.48
F	3.36
G	3.32
H	3.39
I	3.54
8	2.83

A–E, which consist of a macrocycle and tail backbone were predicted as most active and compound **8**, which lacks the tail portion, was predicted as the least active compound. Moreover and in support of our earlier hypothesis regarding the stabilising role of the macrocycle, the predicted values for compounds **F**, **G**, **H** and **I** indicate that the depolymerisation activity can be cumulatively increased for an acyclic analogue through the addition of a cyclic group, which exists in the form of a phenyl ring, in absence of the preferred macrocycle. However, because **F** and **G** are truncated tail analogues, the increase in activity cannot be seen for **G**, as its phenyl ring can only bind at the mouth of the SD1/SD3 cleft and away from the hydrophobic patch. Greater stability and a concomitant increase in activity can be acquired when the cyclic group is closer to the patch, as achieved by compounds **H** and **I** through longer tails. The study by Perrins et al. [52] using tail analogues of reidispongioidide **A** also suggests a small cyclic ring may mimic the contribution of the macrocycle to actin binding as well as increase the affinity of the tail for the binding site.

Table 6 Molecular structures of compounds in the external set

Structure	No.	Substituents			
		R1	R2	R3	R4
	A	H	Me ₃ Ser	H	Me ₂ Gly
	B	H	Me ₃ Ser	Me	Me ₂ Ala
	C	H	Me ₃ Ser	H	MeAla
	D	H	Me ₂ Ser	H	Me ₂ Ala
	E	Me ₂ Ser	H	H	Me ₂ Ala
	F	Me	Me ₂ Ala	—	—
	G	Ph	Me ₂ Ala	—	—
	H	(CH ₂) ₂ Ph	Me ₂ Ala	—	—
	I	(CH ₂) ₄ Ph	Me ₂ Ala	—	—
	8	Me ₃ Ser	—	—	—

Conclusions

Disruption of actin filament dynamics of a deregulated actin system has been identified as a strategy to reverse or perturb the affects of tumour development and progression [9]. The power of several actin-binding natural products, such as the aplyronines, to carry out such functions has qualified the compounds as potential anti-cancer agents. Here, we have identified, through flexible docking studies, potential binding modes of a set natural and synthetic aplyronine analogues to complement and account for the previously published activity data. Most notably, we have shown analogues of the tail portion of the macrolides are able to independently bind at the SD1/SD3 binding cleft on the surface of actin. Moreover, a macrocycle on its own fails to bind to the large hydrophobic patch to which it adheres when a tail is attached, as observed for (+)-end binding macrolides. This result indicates much of the binding specificity of the aplyronine macrolides is attributed to the tail, which is also responsible for the functional activity of these macrolides. The reasonable activity of compound **102** (1 log unit lower than **1**) would support this. Thus, the absence of activity and the inability of the macrocycle part to bind independently to the hydrophobic patch could suggest that the two-phase binding measured for such macrolides [15, 17] commences with the tail binding to the cleft first, followed by the anchoring of the macrocycle on the hydrophobic patch leading into the cleft. This is contrary to the conclusions reached by Klenchin and co-workers [15]. However, our binding studies on G-actin monomers may not reflect the true F-actin severing ability of these compounds and, therefore, it would be difficult to make definite conclusions on this binding mechanism in a full F-actin system. In support of our observations, a recent study on the tail fragment of reidispongionolide A concluded that the actin filament severing function of (+)-end macrolides resides in the tail [52]. Therefore, further work on developing synthetic mimetics of the tail region of these macrolides could help produce more efficacious and tolerable candidate drugs for cancer therapy. Finally, the calculated docking energy scores correlated significantly with the depolymerisation activity for 17 compounds, but only showed a moderate correlation with the cytotoxicity data.

It is important to recognise accurate predictions of ligand binding affinities are not yet possible with scoring functions used by modern-day docking algorithms [53, 54]. The AutoDock scoring function evaluates the change in entropy associated with the loss of torsional freedom for freely rotatable bonds in a ligand, from its unbound to bound state. However, it ignores bonds in cyclic structures. Therefore, we ignored the entropic penalty in comparing the relative binding of macrocycle versus tail fragments

and further investigations will be needed to address this issue more definitively.

The best 3D-QSAR model established a good internal predictive accuracy (q^2 of 0.85) for the depolymerisation activity, using descriptors generated from the four combined property types. Using this model, we made predictions for an external set of ten compounds; the F-actin depolymerisation activity could be measured experimentally using the assay outlined in Kigoshi et al. [20]. Visualisation of the model using contour maps for each property identified key features which influence the activity of the compounds. The maps also indicated several positions on the macrolide where modifications may enhance activity. Hence, the study has provided us with predictive and diagnostic value for the design of a putative set of aplyronine analogues.

Acknowledgments We thank Craig Bruce for advice and useful discussions.

References

- Sheterline P, Clayton J, Sparrow JC (1998) Actin, 4th edn. Oxford University Press, New York
- Carlier MF (1998) Control of actin dynamics. *Curr Opin Cell Biol* 10:45–51
- Carlier MF, Pantaloni D (1997) Control of actin dynamics in cell motility. *J Mol Biol* 269:459–467
- Pollard TD, Borisy GG (2003) Cellular motility driven by assembly and disassembly of actin filaments. *Cell* 112:453–465
- Westphal M, Jungbluth A, Heidecker M, Mühlbauer B, Heizer C, Schwartz JM, Marriott G, Gerisch G (1997) Microfilament dynamics during cell movement and chemotaxis monitored using a GFP-actin fusion protein. *Curr Biol* 7:176–183
- Pollard TD, Cooper JA (1986) Actin and actin-binding proteins: a critical evaluation of mechanisms and functions. *Ann Rev Biochem* 55:987–1035
- dos Remedios CG, Chhabra D, Kekic M, Dedova IV, Tsubakihara M, Berry DA, Nosworthy NJ (2003) Actin binding proteins: regulation of cytoskeletal microfilaments. *Physiol Rev* 83: 433–473
- Stossel TP (1989) From signal to pseudopod. How cells control cytoplasmic actin assembly. *J Biol Chem* 264:18261–18264
- Lambrechts A, Van Troys M, Ampe C (2004) The actin cytoskeleton in normal and pathological cell motility. *Int J Biochem Cell Biol* 36:1890–1909
- Allingham JS, Klenchin VA, Rayment I (2006) Actin-targeting natural products: structures, properties and mechanisms of action. *Cell Mol Life Sci* 63:2119–2134
- Button E, Shapland C, Lawson D (1995) Actin, its associated proteins and metastasis. *Cell Motil Cytoskeleton* 30:247–251
- Giganti A, Friederich E (2003) The actin cytoskeleton as a therapeutic target: state of the art and future directions. *Prog Cell Cycle Res* 5:511–525
- Jordan MA, Wilson L (1998) Microtubules and actin filaments: dynamic targets for cancer chemotherapy. *Curr Opin Cell Biol* 10:123–130
- Yeung KS, Paterson I (2002) Actin-binding marine macrolides: total synthesis and biological importance. *Angew Chem Int Ed Engl* 41:4632–4653

15. Klenchin VA, Allingham JS, King R, Tanaka J, Marriott G, Rayment I (2003) Trisoxazole macrolide toxins mimic the binding of actin-capping proteins to actin. *Nat Struct Biol* 10:1058–1063
16. Spector I, Braet F, Shochet NR, Bubb MR (1999) New anti-actin drugs in the study of the organization and function of the actin cytoskeleton. *Microsc Res Tech* 47:18–37
17. Tanaka J, Yan Y, Choi J, Bai J, Klenchin VA, Rayment I, Marriott G (2003) Biomolecular mimicry in the actin cytoskeleton: mechanisms underlying the cytotoxicity of kabiramide C and related macrolides. *Proc Natl Acad Sci USA* 100:13851–13856
18. Tanaka J, Blain JC, Allingham JS (2008) Actin-binding toxin “tail” wags the dog. *Chem Biol* 15:205–207
19. Hirata K, Muraoka S, Suenaga K, Kuroda T, Kato K, Tanaka H, Yamamoto M, Takata M, Yamada K, Kigoshi H (2006) Structure basis for antitumor effect of aplyronine A. *J Mol Biol* 356: 945–954
20. Kigoshi H, Suenaga K, Takagi M, Akao A, Kanematsu K, Kamei N, Okugawa Y, Yamada K (2002) Cytotoxicity and actin-depolymerizing activity of aplyronine A, a potent antitumor macrolide of marine origin, and its analogs. *Tetrahedron* 58:1075–1102
21. D’Auria MV, Paloma LG, Minale L, Zampella A, Verbist JF, Roussakis C, Debitus C, Patissou J (1994) Reidispongolide A and B, two new potent cytotoxic macrolides from the New Caledonian sponge *Reidispongia coerulea*. *Tetrahedron* 50: 4829–4834
22. Allingham JS, Tanaka J, Marriott G, Rayment I (2004) Absolute stereochemistry of ulapualide A. *Org Lett* 6:597–599
23. Roesener JA, Scheuer PJ (1986) Ulapualide A and B, extraordinary antitumor macrolides from nudibranch eggmasses. *J Am Chem Soc* 108:846–847
24. Yamada K, Ojika M, Ishigaki T, Yoshida Y, Ekimoto H, Arakawa M (1993) Aplyronine A, a potent antitumor substance, and the congeners aplyronine B and C isolated from the sea hare *Aplysia kurodai*. *J Am Chem Soc* 115:11020–11021
25. Suenaga K, Kamei N, Okugawa Y, Takagi M, Akao A, Kigoshi H (1997) Cytotoxicity and actin depolymerizing activity of aplyronine A, a potent antitumor macrolide of marine origin, and the natural and artificial analogs. *Bioorg Med Chem Lett* 7:269–274
26. Saito S, Watabe S, Ozaki H, Kigoshi H, Yamada K, Fusetani N, Karaki H (1996) Novel actin depolymerizing macrolide aplyronine A. *J Biochem* 120:552–555
27. Klebe G, Abraham U, Mietzner T (1994) Molecular similarity indices in a comparative analysis (CoMSIA) of drug molecules to correlate and predict their biological activity. *J Med Chem* 37:4130–4146
28. Burtnick LD, Koepf EK, Grimes J, Jones EY, Stuart DI, McLaughlin PJ, Robinson RC (1997) The crystal structure of plasma gelsolin: implications for actin severing, capping, and nucleation. *Cell* 90:661–670
29. Sun HQ, Yamamoto M, Mejillano M, Yin HL (1999) Gelsolin, a multifunctional actin regulatory protein. *J Biol Chem* 274: 33,179–33182
30. Spartan (2008) Wavefunction Inc., Irvine
31. Halgren T (1996) Merck molecular force field: I–V. *J Comp Chem* 17:490–641
32. Gasteiger J, Marsili M (1980) Iterative partial equalization of orbital electronegativity—a rapid access to atomic charges. *Tetrahedron* 36:3219–3228
33. Sanner MF (1999) Python: a programming language for software integration and development. *J Mol Graph Model* 17:57–61
34. Huey R, Morris GM, Olson AJ, Goodsell DS (2007) A semi-empirical free energy force field with charge-based desolvation. *J Comput Chem* 28:1145–1152
35. Morris GM, Goodsell DS, Halliday RS, Huey R, Hart WE, Belew RK, Olson AJ (1998) Automated docking using a Lamarckian genetic algorithm and an empirical binding free energy function. *J Comput Chem* 19:1639–1662
36. Melville JL, Moal IH, Baker-Glenn C, Shaw PE, Pattenden G, Hirst JD (2007) The structural determinants of macrolide-actin binding: in silico insights. *Biophys J* 92:3862–3867
37. Bottoms CA, White TA, Tanner JJ (2006) Exploring structurally conserved solvent sites in protein families. *Proteins* 64:404–421
38. Ogata K, Wodak SJ (2002) Conserved water molecules in MHC class-I molecules and their putative structural and functional roles. *Protein Eng* 15:697–705
39. Roberts BC, Mancera RL (2008) Ligand-protein docking with water molecules. *J Chem Inf Model* 48:397–408
40. Shaltiel S, Cox S, Taylor SS (1998) Conserved water molecules contribute to the extensive network of interactions at the active site of protein kinase A. *Proc Natl Acad Sci USA* 95:484–491
41. Szybki Version 1.1.2 (2008) OpenEye Scientific Software Inc., Santa Fe
42. Wildman SA, Crippen GM (1999) Prediction of physicochemical parameters by atomic contributions. *J Chem Inf Comput Sci* 39:868–873
43. Hou TJ, Xia K, Zhang W, Xu XJ (2004) ADME evaluation in drug discovery. 4. Prediction of aqueous solubility based on atom contribution approach. *J Chem Inf Comput Sci* 44:266–275
44. Humphrey W, Dalke A, Schulten K (1996) VMD: visual molecular dynamics. *J Mol Graph* 14:33–38
45. Cole JC, Murray CW, Nissink JW, Taylor RD, Taylor R (2005) Comparing protein-ligand docking programs is difficult. *Proteins* 60:325–332
46. Wada S, Matsunaga S, Saito S, Fusetani N, Watabe S (1998) Actin-binding specificity of marine macrolide toxins, mycalolide B and kabiramide D. *J Biochem* 123:946–952
47. Perkins R, Fang H, Tong W, Welsh WJ (2003) Quantitative structure-activity relationship methods: perspectives on drug discovery and toxicology. *Environ Toxicol Chem* 22:1666–1679
48. Rücker C, Rücker G, Meringer M (2007) γ -randomization and its variants in QSPR/QSAR. *J Chem Inf Model* 47:2345–2357
49. Wold S, Eriksson L (1995) In: van de Waterbeemd H (ed) *Chemometric methods in molecular design*. Wiley-VCH, Weinheim, pp 309–318
50. Yamada K, Ojika M, Kigoshi H, Suenaga K (2009) Aplyronine A, a potent antitumor macrolide of marine origin, and the congeners aplyronines B–H: chemistry and biology. *Nat Prod Rep* 26:27–43
51. Kitamura K, Teruya T, Kuroda T, Kigoshi H, Suenaga K (2009) Synthesis of actin-depolymerizing compounds. *Bioorg Med Chem Lett* 19:1896–1898
52. Perrins RD, Cecere G, Paterson I, Marriott G (2008) Synthetic mimetics of actin-binding macrolides: rational design of actin-targeted drugs. *Chem Biol* 15:287–294
53. Leach AR, Shoichet BK, Peishoff CE (2006) Prediction of protein-ligand interactions. Docking and scoring: successes and gaps. *J Med Chem* 49:5851–5855
54. Warren GL, Andrews CW, Capelli A-M, Clarke B, LaLonde J, Lambert MH, Lindvall M, Nevins N, Semus SF, Senger S, Tedesco G, Wall ID, Woolven JM, Peishoff CE, Head MS (2006) A critical assessment of docking programs and scoring functions. *J Med Chem* 49:5912–5931